Visualization and Modelling of Flow Pattern Transitions in a Cross-Corrugated Plate Heat Exchanger Channel with Uniform Two-Phase Distribution

Susanne Buscher

Technische Universität Berlin

Please cite as: ***Buscher, S., Visualization and modelling of flow pattern transitions in a cross-corrugated plate heat exchanger channel with uniform two-phase distribution, International Journal of Heat and Mass Transfer, Volume 144, 2019, 118643,*** https://doi.org/10.1016/j.ijheatmasstransfer.2019.118643.

ABSTRACT

Plate heat exchangers are often used for two-phase applications such as evaporation or absorption. In order to predict heat and mass transfer and pressure drop more accurately, knowledge of flow patterns is essential.

Most of the published flow pattern maps for plate heat exchangers are biased by non-uniform inlet conditions. The objective of this study is to eliminate inlet effects, to which end, a uniform and steady two-phase distribution is implemented.

An adiabatic air-water mixture is visualized in a transparent cross-corrugated single channel. The flow direction is varied between horizontal, vertical upward and downward. Both phases are injected directly into the channel via multiple nozzles. All superficial velocities are determined for the actual operating conditions.

Flow patterns are mostly not affected by flow direction. Instead, the centrifugal force often dominates over buoyancy due to the swirling flow induced by the corrugations. A corrugation Froude number is defined to explain the findings. So-called slug flow is not observed, although being reported by other authors. This is attributed to the inlet design.

Simple model assumptions regarding flow pattern transitions in tubes are adapted to the cross-corrugated channel. An additional model is proposed to account for the gradual transition of flow patterns at higher void fractions. The minimum kinetic energy for bubble breakage is also modelled to explain the gas accumulation observed at slow down-flow.

Keywords: plate heat exchanger; flow pattern; visualization; modelling; flow direction; maldistribution

1. INTRODUCTION

Plate heat exchangers are used as evaporators/condensers or absorbers/desorbers in refrigeration processes and other applications providing excellent heat transfer in a small volume. Most of the industrial plate heat exchangers consist of chevron or herringbone-type plates forming cross-corrugated channels.

Numerous correlations exist for two-phase pressure drop and heat transfer in plate heat exchangers regarding condensation [1], evaporation [2] and absorption [3–5]. Most correlations, however, are limited with respect to plate design, experimental conditions and working fluids. In contrast, research on flow patterns and development of separate correlations for them have been suggested [6–13] in order to yield more accurate predictive models. Those types of correlations could be applied to incremental models of plate heat exchangers taking into account that phase changing fluids go through various flow patterns. For this purpose, however, the fluid mechanics creating the flow patterns need to be understood. Models predicting flow patterns should be available and empirically validated. To the knowledge of the author, such models have yet not been published for cross-corrugated channels. It is the purpose of the current paper to fill this gap.

1.1. Objectives and Outline of the Study

The present investigation focuses on the fundamental behaviour of two-phase flow passing through a cross-corrugated channel. Modelling of flow pattern transitions is proposed and verified using own experimental data.

The experimental setup is designed to yield flow patterns in cross-corrugated channels under idealized conditions such as uniform and steady two-phase distribution across the channel width, absence of contaminants and non-interference of heat and mass transfer. Of course, industrial processes are not of this quality. However, in order to identify the underlying principles, all other influences need to be either disabled or controlled. Therefore, the experimental layout eliminates maldistribution from portholes by injecting gas and liquid via separate nozzles. The impact of buoyancy is examined by varying the flow direction of the channel. Air-water flow is used as an adiabatic model system, as is common in literature. Special emphasis is given to clarify the state variables applied for the gas phase, which were often not specified in the literature.

Simple model assumptions are proposed in order to account for the observed flow pattern transitions in the cross-corrugated channel. Most of the assumptions are based on the flow-pattern modelling developed for tubes in several articles by Taitel, Barnea et al. [14–16]. However, differences regarding geometry and the impact of buoyancy demand for modifications. The proposed model assumptions are given as simple equations and are supposed widely applicable, provided that channel geometry enforces a swirling two-phase flow (see section 4.1). Since knowledge of the operating conditions is required, the proposed flow-pattern modelling is hoped to be integrated in prospective incremental models of plate heat exchangers which also incorporate heat and mass transfer and pressure drop.

The introductory part of this study continues with a literature review regarding flow patterns and two-phase distributions in plate heat exchangers. In section 2, the experimental layout is described in detail. The observed flow patterns are defined in section 3. After that, the swirling motion of the two-phase flow is addressed in section 4. In the same section, the corrugation Froude number is introduced to quantify centrifugal forces in comparison to buoyancy. The experimental flow pattern maps are presented and discussed in section 5. Subsequently, section 6 proposes the flow-pattern transition modelling. At last, section 7 summarizes the main outcomes of this study.

1.2. Literature Review: Flow Patterns in Plate Heat Exchangers

Flow patterns have been visualized in cross-corrugated channels by several researchers. Recently, the state of the art has been summarized in [7,11]. This literature review focuses on the aspects formulated as questions i) to iv). The answers are summarized below and displayed systematically in Table 1. The most relevant studies are discussed with more detail further below.

i) Which flow directions and which fluids were visualized? What plate types were used?

ii) Which oscillating flow patterns were described and how?

iii) What did channel inlet and mixer look like? Which observations were reported in them?

iv) Which pressure and temperature values were used to determine the gas superficial velocities? Were those parameters measured in or near the channel?

In most of the reviewed studies, listed in Table 1, flow direction was vertical upward or downward. Apart from the current study, only Shiomi et al. [17] investigated horizontal flow. Asano et al. [18] observed that flow direction influenced two-phase distribution. Yet, the impact of flow direction on flow patterns in plate heat exchangers has not been systematically investigated.

All cited studies used air-water mixtures. Authors who investigated different fluids also compared the results to air-water flow. In most studies, two-phase flow was adiabatic; only Nilpueng and Wongwises [19] heated the air-water mixture and Yang et al. [20] evaporated R410A.

Except for Jiang and Bai [21], all researchers chose cross-corrugated channels. The impact of corrugation angles on flow patterns was shown by Tribbe and Müller-Steinhagen [9] who reported a clear effect, while Grabenstein et al. [6,7] could not verify a significant influence.

Most of the reviewed experiments kept the inlet region of the original plate and mixed both phases in a T-joint prior to injection. However, Grabenstein et al. [6,7] installed a mixing chamber adjacent to the channel, as did Jiang and Bai [21]. Yang et al. [20] injected the air separately into the channel. They were the only ones who did not report oscillating flow – although flow patterns were not their research focus. Two-phase maldistribution in the inlet port was reported by Vlasogiannis et al. [10] and Asano et al. [18,22]: Slugging or phase separation in the inlet pipe were blamed for so-called slug flow and maldistribution in the channel, respectively. In contrast to the current study, none of the published research could get rid of inlet effects; thus, none of them produced uniform and steady two-phase distributions at all combinations of flow rates.

Except for Vlasogiannis et al. [10] who chose standard conditions, it was usually not explicated which pressures and temperatures were implied for superficial gas velocities. Also, pressure or temperature measurement, in or near the channel, was often not reported (see Table 1). Therefore, it is possible that some or maybe all of the other cited studies also assumed standard conditions. However, due to varying pressure drop and hydrostatic pressure, the operating pressure inside the channel is not constant and can deviate significantly from standard conditions, affecting gas density. Using constant values to calculate superficial gas velocities, therefore, could cause distortion of the flow pattern maps. Also, employing standard conditions would result in different flow pattern maps for the same channel when operated at different pressures.

The introductory literature on two-phase flow, such as [33], does not specify which temperature and pressure to use when calculating the superficial gas velocity. However, the literature also defines the homogeneous void fraction, assuming both gas and liquid to move at the same speed without slip. This void fraction is calculated by volumetric flow rates or superficial velocities, see Eq. (6) in section 6.1. Being coherent, the actual operating conditions are to imply for the gas phase. Moreover, slip and interfacial friction depend on the actual gas volume partly blocking the channel and forcing the two phases to accelerate. Also, probabilities of bubble coalescence and breakage relate to real bubble volumes.

Vlasogiannis et al. [10] reported that the occurrence of slug flow was sensitive to the inlet conditions: Slugging in the channel coincided with slugging in the inlet pipe which was observed at the inlet porthole through the transparent plate. In a second experiment, the authors investigated the influence of flow patterns on heat transfer by heating the air-water mixture in a plate pack.

Table 1. Systematic literature review (alphabetical): Answers to questions i)-iv) of section 1.2

	Plate type, fluid, flow direction (i)	Description of oscillating flow pattern (ii)	Mixer and inlet design, observations at inlet (iii)	Gas phase: pressure and temperature (iv)
Asano et al. [18,22]	herringbone [22]; chevron [18]; adiabatic air-water and boiling R141b up-flow [22]; air-water up- and down-flow [18]	varying two-phase distribution along channel length	porthole diameter deduced from pictures ~50 mm; de-mixing at inlet cause maldistribution; unsteady void fraction at inlet cause varying two-phase distribu-tion along channel length	not specified; pressure and temperature measured for the boiling flow, but not for air-water; no flow pattern map
Grabenstein et al. [6,7,13]	double herring-bone (63°, 27°); adiabatic air-water down-flow; condensing R365mfc	"slug flow": periodic liquid torrents perpendicular to flow direction	8 mixing nozzles leading to a mixing chamber (shaped as reclined cylinder) attached to channel and with a horizontal metal grid for homogenization	not specified; constant densities of air and R365mfc given; operating pressure and temperature measured
Jiang and Bai [21]	capsule-type with ellipsoidal embossing; adiabatic air-water down-flow	"churn flow": fast-moving liquid torrents containing bubbles and spreading over whole channel width	liquid injected at 10 inlets to mixing volume attached to channel, 1 gas inlet; no observations in transparent mixing section reported	not specified; pressure measured at channel inlet, but not temperature
Nilpueng and Wongwises [19]	asymmetrical mixed-angle herringbone; heated air-water; up-flow, down-flow	"slug flow" only in down-flow: alternating full water and full air flow similar to slug flow in tubes	T-joint; porthole Ø 30 mm; viewing window not included port holes; maldistribution at low flow rates in downward flow	not specified; temperature measured at inlet and outlet, but not operating pressure
Shiomi et al. [17]	chevron (60°, 30°, 30°/60°); adiabatic air-water upward, horizontal	not reported	not specified; pictures of channel showed maldistribution	not specified
Tribbe and Müller-Steinhagen [9]	herringbone (60°, 30°, 30°/60°); adiabatic air-water down-flow	"churn flow": high-velocity liquid slugs with fine bubbles travelling along hole channel, alternating with quiescent film flow	T-joint 350 mm before inlet; dispenser: 3 orifices each Ø 5 mm (60 mm before inlet); porthole Ø 50 mm; inlet ports were covered	not specified; pressure and temperature measured at inlet and outlet
Vlasogiannis et al. [10]	herringbone (60°); adiabatic air-water down-flow	"slug flow": sharp fronts orthogonal to flow direction extend over channel width, separate bubbly region from film flow region	T-joint 1800 mm before inlet; tube Ø 36 mm; slug flow in the channel coincides with observed slugging in inlet pipe	standard conditions (1 atm, 25 °C)
Winkelmann [12]	herringbone (27.5°); adiabatic air-water down-flow	"churn flow": rapid periodic changes of local two-phase distribution, liquid waves with small bubbles alternate with gas pockets	porthole Ø 49 mm; viewing window not included port holes; maldistribution at low flow rates	not specified; air volume at standard conditions; operating pressure measured, but not temperature
Yang et al. [20]	chevron (65°); adiabatic air-water upward flow; evaporating R410A (infrared thermography)	not reported	separate injection of air at varying points at porthole; partially evaporated R410A via a nozzle of Ø 3 mm at same locations; porthole diameter ~50 mm	not specified for air; operating pressure and temperature not measured for air, only for R410A; no flow pattern map
this study	chevron (75°); adiabatic air-water horizontal, upward and downward flow	no oscillating flow patterns resembling descriptions in literature; at high gas flow rates: pressure fluctuations and locally varying waviness in full film flow	low gas flow rates: separate injection via 8 nozzles per phase; high gas flow rates: pre-mixing in 8 T-joints 110 mm prior to injection	assumed humid air at operating pressure halfway of the channel length and temperature measured at the outlet

Asano et al. [22] used non-transparent plates and neutron radiography for visualization. Gas-liquid distributions were analyzed by image processing. Maldistributions at the inlet were not compensated for when the mixtures passed through the channel. Separation of gas and liquid at the inlet induced asymmetrical distributions. Unsteady void fractions were caused by slugging in the inlet pipe and carried on throughout the channel. The authors concluded that the commonly large portholes are responsible for the de-mixing of the phases. Asano et al. [18] also compared upward and downward flow direction. At low liquid flow rates, the gas phase concentrated in the middle in up-flow whereas it was diverged to the sides in down-flow. This effect is attributed to the locations of the phases in the inlet port with respect to the plate center.

Yang et al. [20] varied the point of gas injection around the inlet porthole. Upward air-water flow achieved the best two-phase distribution when air was injected opposite to the flow direction. The inlet point directly in flow direction produced significant maldistribution. The impact of two-phase Reynolds numbers on distribution was low compared to the variation of injection points. Partially evaporated R410A was heated by water in a three-channel heat exchanger. The water temperature was visualized by infrared thermography. The heat transfer performance was best when that injection point was used which produced the significant maldistribution in air-water flow.

Tribbe and Müller-Steinhagen [8,9] aimed at avoiding maldistribution and oscillations caused by stratified flow and slugging in the horizontal inlet pipe. Therefore, they placed a mixing section with three 5-mm orifices at a distance 60 mm upstream of the channel inlet [8]. Since Tribbe and Müller-Steinhagen [9] did not report maldistribution, the mixer probably was successful preventing stratified flow. However, slugging was presumably not avoided because the described mixing section is unlikely to homogenize periodic changes of gas-liquid concentrations which are typical for slug flow. The authors did not relate their observed oscillating “churn flow” to possible slugging in the inlet pipe. Their flow pattern maps also differed with respect to the corrugation angles and showed a larger churn-flow region for the higher angle. The authors did not mention at which pressures and temperatures they calculated the superficial gas velocities. If constant values were used, however, deviations in the flow pattern maps could be attributed in part to a change of operating pressure inside the channel due to the impact of corrugation angle on pressure drop.

Grabenstein et al. [6,7] were the only ones who constructed flow pattern maps for cross-corrugated channels based on momentum flux. They compared their results to other air-water flow pattern maps [9,10,12] originally published in terms of superficial velocities. The authors did not state how they converted the axes to momentum flux, but it seems possible that the standard air density was used, which was reported as a fluid property. Since not specified otherwise, this value maybe was implied for the empirical gas momentum flux, too. Grabenstein et al. [6,7] also investigated two-phase pressure drop and proposed a model connected to the observed flow patterns. However, the presumed state variables of the gas phase affect void fraction, mean density and the hydrostatic pressure used to determine vertical two-phase pressure drop.

Grabenstein et al. [7] referred to [9,12] which reported oscillating flow patterns with a porthole inlet condition, thus, arguing that their “slug flow” was not “homemade” by the mixer design. However, other studies [10,22] explicitly made inlet conditions similar to those in [9,12] responsible for oscillating flow patterns. Therefore, the argumentation is not convincing. The mixer design is described with much detail by Grabenstein [6] (pp. 30, 43): Gas and liquid phase are mixed in 8 nozzles leading to a mixing chamber adjacent to the channel entrance and equipped with a metal grid for homogenization. However, a grid is unlikely to prevent coalescence of gas bubbles and subsequent phase separation due to gravity. Also, it would not compensate for pressure oscillations which could emanate from other parts of the test plant, such as slug flow in subsequent piping or waves in the water tank. If such pressure fluctuations had occurred, the gas phase in the mixing chamber maybe was quickly compressed and decompressed pushing varying amounts of water and gas into the channel. Thus, it is possible that the observed slug flow originated in the mixing chamber.

In a review article, Tao et al. [11] combined several published flow pattern maps of downward flow [7,9,10,12,13,19]. The authors developed dimensionless numbers in order to relate flow patterns in cross-corrugated channels to those in mini-tubes. Although the general tendencies were similar, the individual transition lines of the studies did not match each other – either displayed in terms of dimensionless numbers or using the original superficial velocities (momentum flux of [7] was converted). Tao et al. [11] gave the following reasons: subjectivity of flow pattern definitions and classification; varying quality of visualization; different types of inlet distributors and unclear operating conditions. The authors incorporated many unknowns, such as assumed operating conditions, into the conversion of the published data to dimensionless numbers. However, the operating pressures were maybe not constant and not only depending on pressure drop, as assumed by Tao et al. [11]. Also, unknown hydrostatic pressures were presumably imposed by individual plant designs. Therefore, the dimensionless flow pattern maps are receptive for additional bias introduced by the assumptions, as was also indicated by the authors.

Jiang and Bai [21] investigated a transparent single channel made of capsule-type plates characterized by ellipsoidal embossing. Similar to the approach of this study, the authors modelled flow pattern transitions referring to the modelling developed for tubes by Taitel, Barnea et al. [14–16]. However, since their channel enabled straight passages, the impact of buoyancy and slip was supposedly strong, similar to tubes. In contrast, cross-corrugated channels enforce a swirling motion on two-phase flow which often minimizes the impact of buoyancy and hinders slip (see section 4.1 and [23]). Thus, it is not surprising, that the flow-pattern modelling of Jiang and Bai [21] differs a lot from the assumptions proposed in this study, as do the reported flow patterns. Therefore, their modelling is not expected to account well for cross-corrugated channels. However, Jiang and Bai [21] compared their flow pattern transitions with those for cross-corrugated channels in [9] and [7]. For unknown reasons, the supposedly same transition lines of [9] and [7] were close to each other in [21], but they differed when compared by Tao et al. [11], as did the original studies.

Approaches to model two-phase heat and mass transfer based on flow patterns are rarely published for plate heat exchangers. This could be attributed to the lack of appropriate flow-pattern models. Cerezo et al. [4,24] modelled absorption in a corrugated plate heat exchanger only for bubbly flow. Kang et al. [25] modelled absorption in a plate heat exchanger channel. They presupposed bubbly or film flow, respectively, which was assumed to pass a flat channel.

2. LAYOUT OF THE EXPERIMENT

2.1. The Cross-Corrugated Single Channel

A transparent cross-corrugated single channel is pivot-mounted to vary flow direction and study the impact of buoyancy. To achieve a uniform and steady two-phase distribution, the typical inlet region of heat exchanger plates is substituted by nozzles for separate injection of gas and liquid. The experimental facility was briefly outlined in [26], but is described with more detail at this point.

The cross-corrugated channel consists of two transparent polycarbonate plates, each 20 mm thick. A sinusoidal corrugation profile was micro-milled into both plates. The mean surface roughness is less than 12 µm. The geometric properties of the cross-corrugated channel are listed in Table 2. The hydraulic diameter was calculated according to Martin [27].

Table 2. Geometric properties of the cross-corrugated channel

Corrugation angle	ϕ	75°	Hydraulic diameter	D_h	4.14 mm
Corrugation depth (amplitude)	a	1.2 mm	Channel width	B	278.2 mm
Wave length	λ	9 mm	Channel length	L	326.1 mm

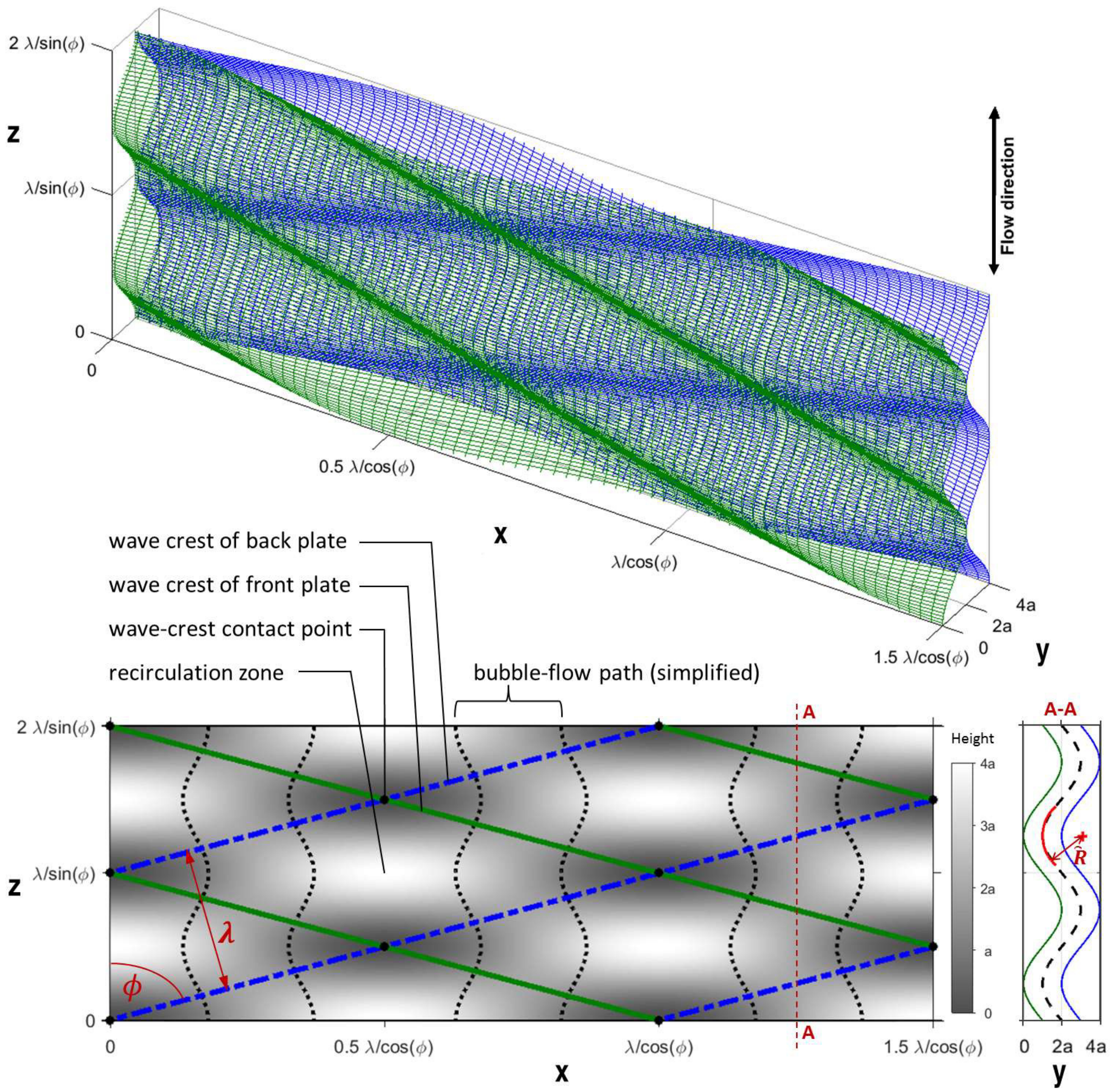

Figure 1 – top: 3D-representation of the sinusoidal profiles of both plates (cut-out);
– bottom left: 2D-projection of top diagram with grey shades denoting local channel height;
– bottom right: Cross-section between two rows of wave-crest contact points (zy-plane)

The cross-corrugated channel is formed by two wavy profiles with the amplitude a (corrugation depth) as displayed in the top diagram of Figure 1. It illustrates that the local height varies between 0 mm at the wave-crest contact points, where both profiles touch, and the maximum of $4\,a = 4.8\,mm$. The 3D-representation of the top diagram is projected into the xz-plane as shown in the bottom left diagram of Figure 1. There, the wave length λ and the corrugation angle ϕ, with respect to flow direction, are designated. As channel height is indicated by grey shades, the dark areas denote the narrow regions near the wave-crest contact points while the bright areas in-between represent the larger recirculation zones. The main portion of the two-phase mixture passes through the flow path sketched by the dotted lines (section 4.1). The bottom right diagram of Figure 1 is a cross-section in the yz-plane in the middle of this flow path, showing constant channel height there.

On each side of the channel, compressed air is filled in a transparent pressure chamber which is built from an additional transparent plate and a frame of Viton sealing, see Figure 2. Thus, the corrugated plates are pressed against each other by 4 bar(g) in order to prevent deformation and secure contact of the wave crests of both plates.

The main objective of the channel inlet design is to obtain a uniform gas-liquid distribution across the channel width and to avoid coalescence or slugging of the gas phase before entering the channel. The injection and mixing of the two phases take place in two different ways: For low gas flow rates, both phases are injected separately into the channel via 8 nozzles per phase. The nozzles for gas and liquid are located opposite to each other to facilitate intense mixing, see Figure 2. Since each nozzle is drilled into a wave trough, the width of the channel is set to 8 corrugations perpendicular to flow direction: $B = 8 \cdot \lambda / \cos(\phi)$.

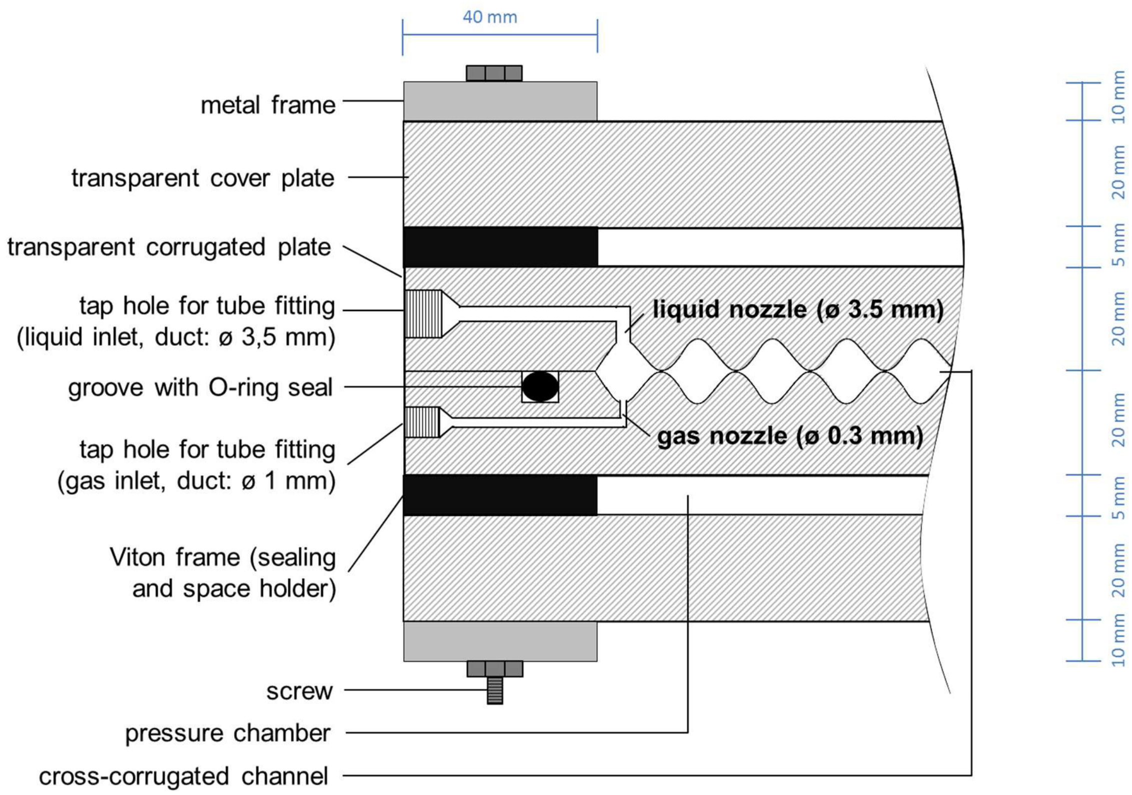

Figure 2: Schematic cross-section of separate gas and liquid inlet nozzles of the single channel

At higher gas flow rates, the gas and liquid phase are pre-mixed in the 8 inlet tubes of the liquid while the gas nozzles are closed. Both gas-injection methods are displayed schematically in Figure 3. To compare the methods, experiments are conducted in both ways for superficial gas velocities ($c_{S,gas}$) from 0.06 m/s to 0.3 m/s. In some cases, pre-mixing performs slightly better, as will be discussed later. However, pre-mixing is not able to provide a uniform two-phase distribution for $c_{S,gas} < 0.06\, m/s$, whereas high frictional pressure drop in the fine gas nozzles rules out separate injection for gas superficial velocities of $c_{S,gas} > 0.3\, m/s$.

A digital camera with high resolution (36 MP) is used to make photographs of the whole channel which is evenly illuminated by flat-panel LEDs from the back. As shown by the photographs inserted in Figure 3, both injection methods finely disperse the gas phase at the entrance into many small bubbles rapidly coalescing and forming a stable flow pattern after a short entry length.

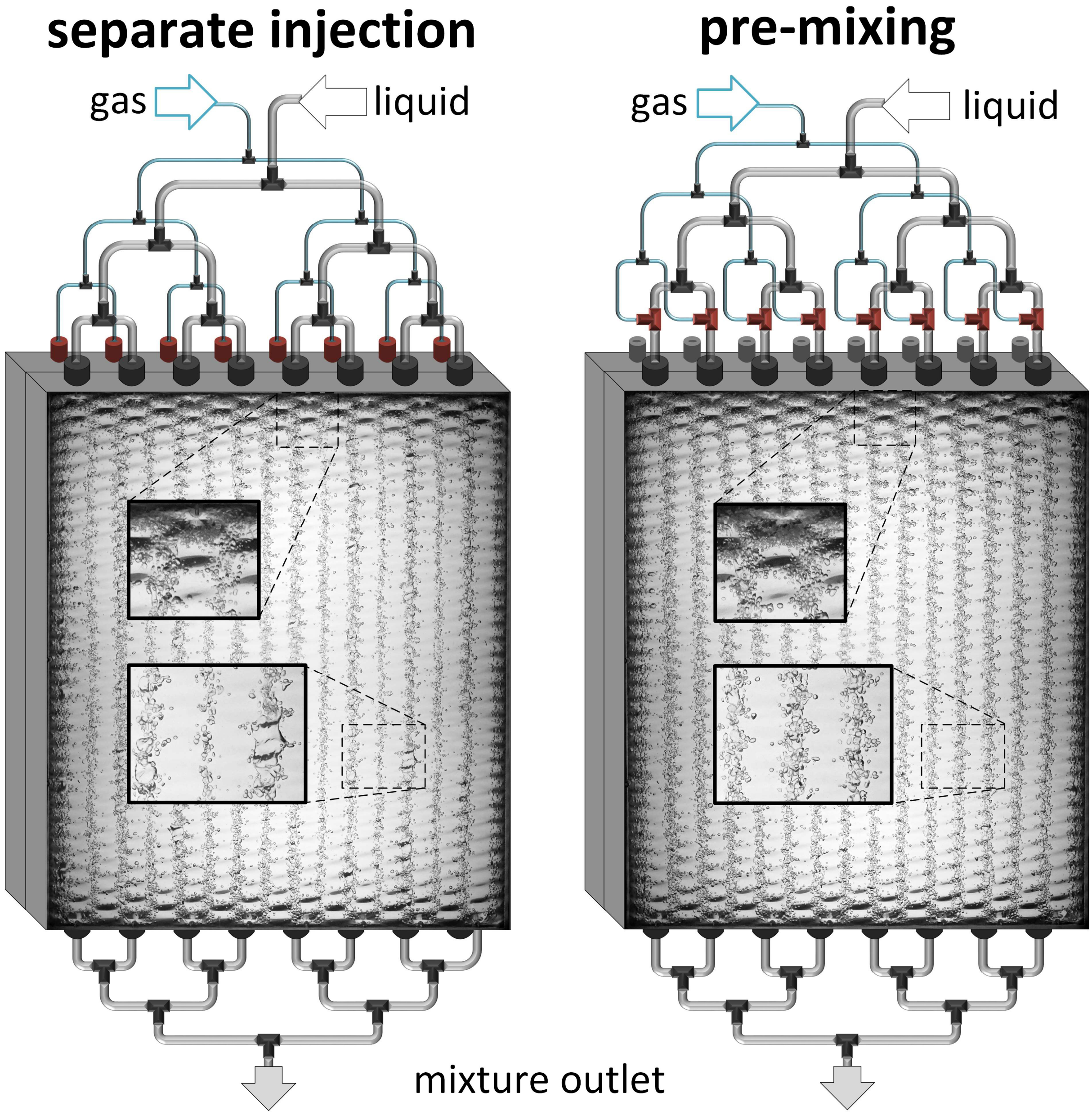

Figure 3: Schematic representations of the two gas-injection methods. In the centres: photographs of two-phase flow produced with respective method (both: horizontal, $c_{S,liq}$ = 0.28 m/s; $c_{S,gas}$ = 0.12 m/s).

2.2. The Test Plant and Pulsating Flow

The liquid phase is deionized water which is re-circulated by a centrifugal pump. The maximum conductivity was 1 µS/cm, as measured with a conductivity meter.

Pressurized air represents the gas phase and is separated from the liquid in the storage tank. The absolute gas volumetric flow rate is calculated from mass-flow measurements by means of temperature, measured in the outlet stream, and absolute pressure, which is the sum of ambient pressure and gauge pressure. The gauge pressure is measured at a borehole of 0.3 mm, similar to a gas nozzle shown in Figure 2, but located halfway of the plate length at the side of the cross-corrugated channel. Differential pressure is also measured within in the channel via another set of small boreholes, but these measurements are not discussed here, see instead [23].

The operating conditions are in the following limits: The absolute pressure ranges from 1.3 bar to 2.2 bar, due to the high pressure drop of the inlet and outlet design. Temperatures range from 19 °C to 23 °C. Differential pressure varies from 8 mbar to 182 mbar in horizontal two-phase flow [23].

In preliminary experiments, large pressure oscillations were recorded which in part influenced the flow patterns in the cross-corrugated channel, particularly at high gas flow rates. The oscillations were attributed to intermittent flow phenomena in different parts of the test plant, for instance slug flow in the return pipes and waves in the storage tank, which were caused by intermittent return flow in the inlet to the tank and which could have affected the steady-state condition of the pump. The fluctuations were completely eliminated when the outlet stream was discarded into a bucket right after leaving the channel in downward flow. However, this mode of operation was not feasible in order to make the desired measurements.

While slug flow cannot be prevented entirely in the test plant, the tube orientation and diameter can influence the onset of slugging. Furthermore, Wu et al. [28] stated that slug flow was unlikely to form in tubes with diameters above 100 mm. Therefore, the vertical upward return pipe to the storage tank is replaced by a tube of 100 mm diameter. Barnea [16] reported that slugging in vertical downward flow occurred less often compared to upward or horizontal flow in the same tube. Therefore, unnecessary horizontal or upward tubing is eliminated from the test plant where possible. In the storage tank, a special inlet design prevents the two-phase return flow from disturbing the water surface. Interference between possible oscillating phenomena and mass-flow controller of the pump is precluded by adjusting liquid flow manually with a valve.

2.3. Uncertainty Analysis

The volumetric flow rate of water is measured with a nutating disc meter (accuracy 1.5% of reading). The water conductivity is measured with a hand-held conductivity meter after each test run (range 0…2 μS/cm or 0…20 μS/cm; accuracy 1.5% of range).

Two mass flow controllers are used to measure dry filtered air (Bronkhorst F-202AV, F-201CV; accuracy 0.5% of reading plus 0.1% of range). The ranges of both devices are adjustable (min. 0.01...0.77 l_n/min; max. 2.5…160 l_n/min). The two-phase outlet temperature is measured with a calibrated PT100 (class B). The gauge pressure is measured in the middle of the channel by a digital manometer (range of 3 bar, accuracy 0.1% of range). Atmospheric pressure is taken from weather data (with 10 mbar uncertainty assumed). Differential pressure measurement had also variable ranges (max. 0…150 mbar; min. 0...2.5 mbar, accuracy 0.1% of range).

The dry air is assumed be saturated to 90% (±10%) immediately after entering the channel. The vapour pressure is determined for the outlet temperature. While the decrease of liquid volume by evaporation is neglected, the vapour volume is determined to increase accuracy of the gas flow. Thus, the volumetric flow rate of humid air increases by 1% (at 19 °C and 2.2 bar) to 2% (at 23 °C and 1.3 bar) compared to dry air.

The expanded uncertainties of the experimental data are obtained according to JCGM 100:2008 [29]. They include accuracies of devices and data acquisition, standard deviations, uncertainty of material properties and error propagation. In conclusion, the volumetric flow rates have a maximum expanded uncertainty of 1.7% for water and of 4.8 % for (humid) air at operation conditions. The maximum expanded uncertainties of the superficial velocities are assumed for liquid and gas as 3.2%, and 5.5%, respectively, taking into account 2.7% expanded uncertainty of the channel cross-section due to manufacturing limits. The homogeneous void fraction and the corrugation Froude number (see section 4.2) have maximum uncertainties of 4.7% and 10%, respectively.

3. FLOW PATTERN CLASSIFICATION

Flow patterns depend on channel geometry, and their observation is influenced by the visualization method, i. e. transparency and lighting [11]. The distinction of flow patterns is biased by the subjectivity of the person interpreting the data and the definitions of the flow patterns. Also, the distribution of measurement points in relation to the measurement range might influence whether a small number of rough flow patterns is defined or additional transition-flow patterns are introduced.

3.1. Bubbly Flow (b, B)

Bubbly flow is subdivided into two categories: Predominantly roundish – but not necessarily completely round – bubbles (b) are clearly smaller than one corrugation. In contrast, irregular blob-like bubbles (B) frequently are bigger than one corrugation but not several corrugations long and without zigzag shape. Examples of both types are shown in Figure 4.

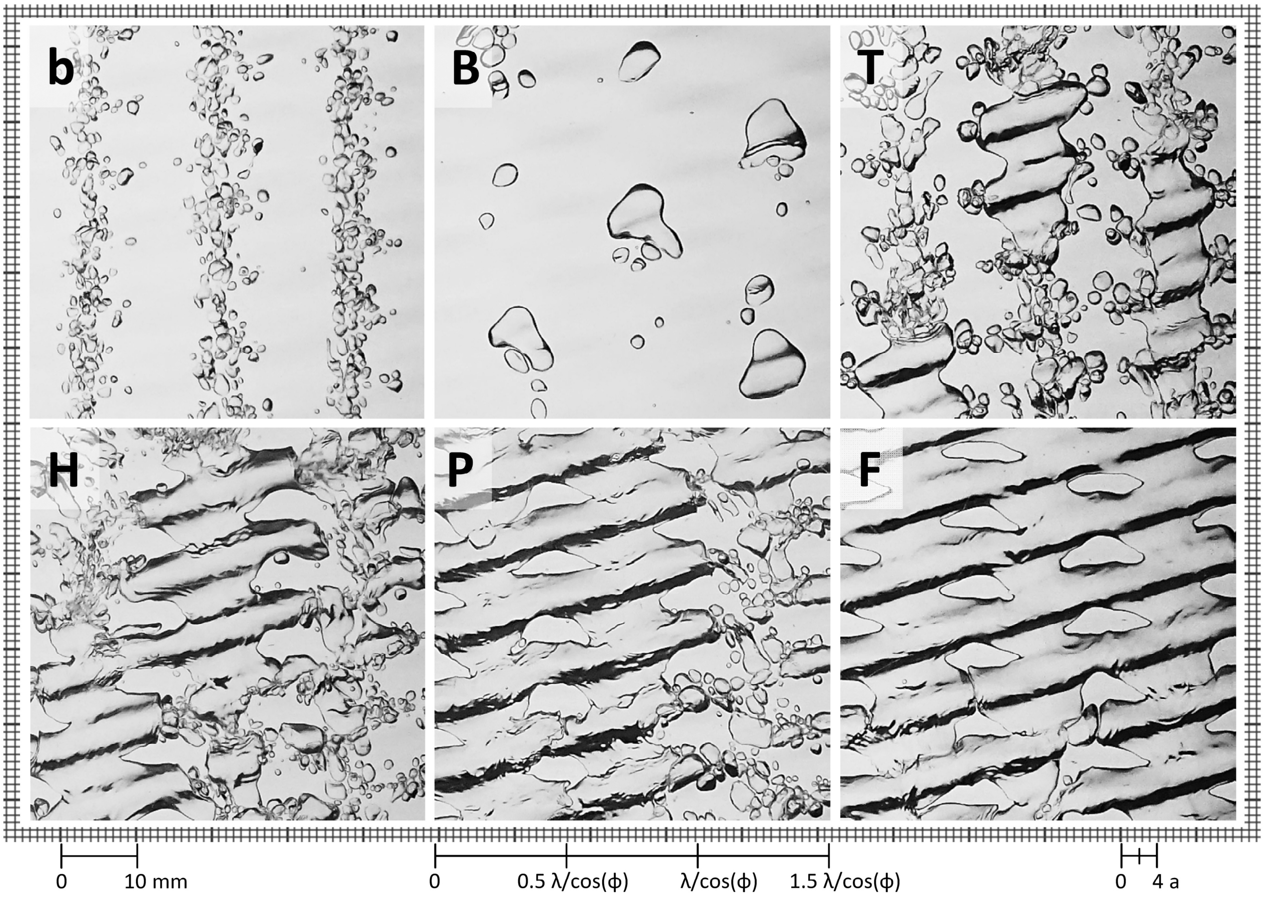

Figure 4: Examples of flow patterns (details). b: small bubbly, B: blob-like bubbles, T: Taylor-like bubbles, H: heterogeneous flow; P: partial film flow, F: full film flow.

3.2. Intermediate Flow (T, H, P)

The transition from bubbly to film flow expands gradually over a large area of the flow pattern map. The intermediate flow patterns are defined to describe the different stages of transition.

Intermediate flow begins when many bubbles combine to form bigger gas units (T), while bubbles are still predominant in the rest of the flow. The big gas units are often several corrugations long and zigzag-shaped. In Figure 4, the corrugations become apparent as dark shadow lines at the liquid film surrounding the gas phase. The big gas units are termed “Taylor-like bubbles” because – similar to Taylor bubbles in tubes – their zigzag-shape is determined by the channel geometry, i. e. the corrugations and the distances between the contact points of the wave crests. The Taylor-like bubbles expand over most of the cross-section between two rows of wave-crest contact points. They seem to fill out the “bubble-flow path” schematically shown in the bottom left diagram of Figure 1. Wakes of smaller bubbles seem to follow the Taylor-like bubbles, see also Figure 5 (third row) comparing the pictures of upward and downward flow.

Adding more gas makes the Taylor-like bubbles bigger and longer. When their combined area extends over about 40% of the projected area of the two-phase flow, the flow pattern is classified as heterogeneous flow (H). Then, the large gas units start to converge and to extend into the recirculation zones behind the wave-crest contact points, see the bottom left diagram of Figure 1. The gas units are not considered as separate entities anymore, but as regions of local film flow.

If the local film flow regions extend in width and enclose several wave-crest contact points, while some limited regions of bubbly flow are still present, it is classified as partial film flow (P).

In Figure 4, the wave-crest contact points and the local film flow regions are distinguished as follows: The pure liquid is always brighter than the gas phase. The wave-crest contact points, therefore, are highlighted by the surrounding liquid, see H, P and F in Figure 4. The local film flow regions in H, P and F are identified by the shadows of the corrugation profile.

3.3. Full Film Flow (F)

If the local film flow is predominant, it is classified as full film flow (F). However, local bubbly flow up to about 10% of the projected area of two-phase flow is permissible. The bubbles usually are attached to the local film flow regions, probably just before coalescing with or after separating from the continuous gas phase.

3.4. Stagnant Gas Phase (S)

One flow pattern only occurs at very low gas and liquid flow rates in vertical downward flow: Big stagnant bubbles (S) rest in the recirculation zones behind the wave-crest contact points, both denoted in the bottom left diagram of Figure 1. A liquid rivulet slowly flows down following the “bubble-flow path” and carrying a few smaller bubbles which only represent a fraction of the gas phase in the channel. An example of this is shown in the top right picture of Figure 5.

4. THE CENTRIFUGAL FORCE

4.1. The Helical Flow Path

For most cases of bubbly flow and Taylor-like bubbly flow, the gas phase concentrates in longitudinal wavy flow paths each between two rows of wave-crest contact points. They are termed “bubble-flow paths”, schematically illustrated in the bottom left diagram of Figure 1.

The effect is striking for all flow directions and in most cases seems to dominate over gravity [26]. Examples are shown in Figure 5 comparing photographs of two-phase flow at similar superficial velocities and varying flow directions. In the second and third row of Figure 5, the gas concentrates in the bubble-flow paths at all flow directions. In the first row of Figure 5, however, the gas phase is distributed differently depending on the flow direction; this is attributed to dominance of buoyancy in this case.

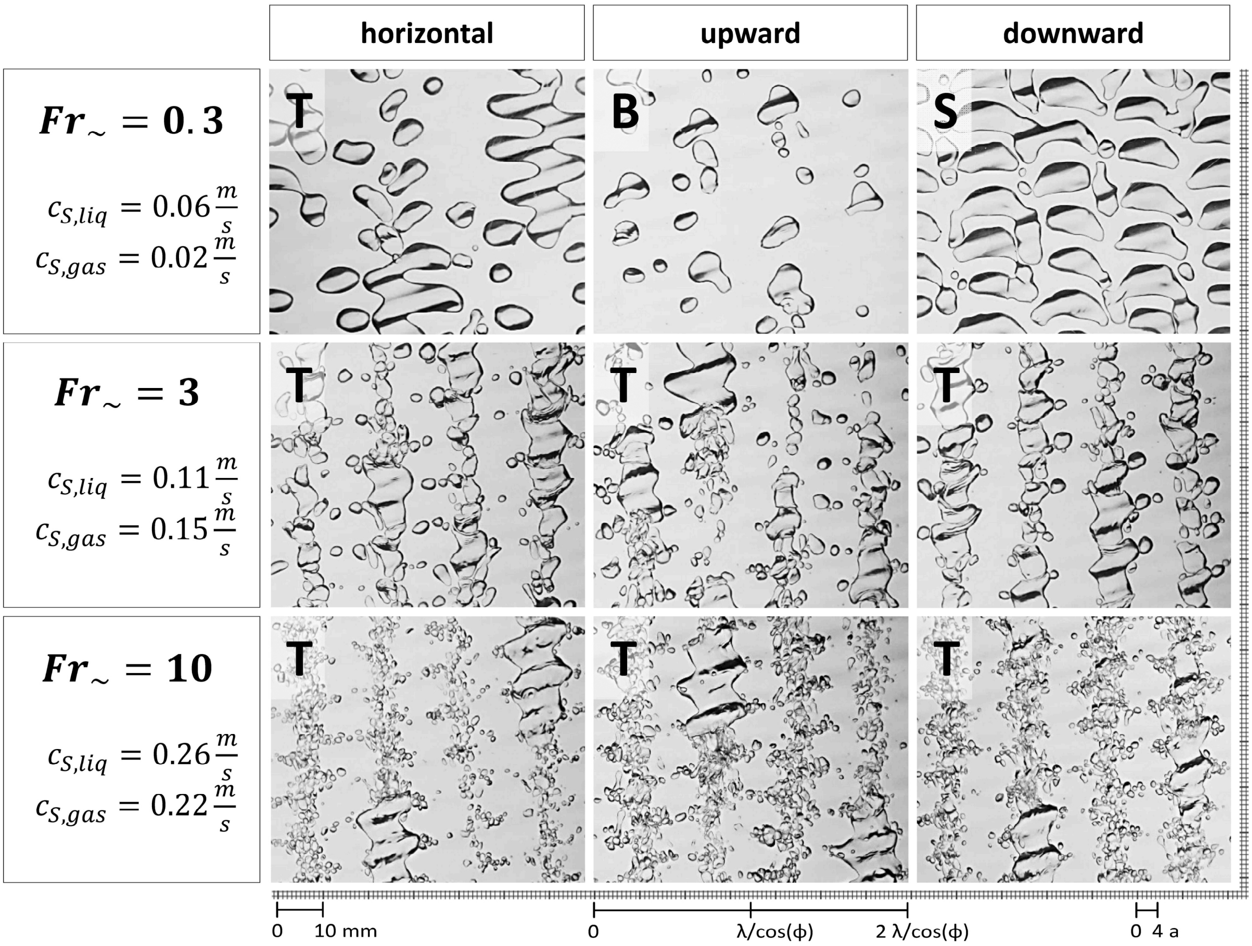

Figure 5: Corrugation Froude number: Effect of centrifugal force vs. buoyancy on flow patterns

Tribbe and Müller-Steinhagen [9] also reported gas bubbles to follow a longitudinal wavy flow path in a plate heat exchanger with a corrugation angle of 60°. They did not investigate the impact of flow directions and velocities on this phenomenon. For a corrugation angle of 30°, however, the two-phase flow was observed to follow the furrows of the corrugations, so-called crossing flow.

Using colour experiments, Focke and Knibbe [30] showed single-phase liquid flow to follow a helical flow path in the case of a high corrugation angle of the plate profile. They concluded that the flow is “reflected” close to the wave-crest contact points. At low corrugation angles, crossing flow was also observed.

Empirical investigations of two-phase flow in tube bends [31,32] showed that the centrifugal force causes the lighter phase to be oriented towards the inner radius of the bend. This effect often was dominant over buoyancy.

Since the two-phase flow in the present cross-corrugated channel is understood to follow a helical flow path, similar to single-phase flow, centrifugal forces constantly affect the two phases. The proportion of the centrifugal force to buoyancy is quantified below in order to explain the variable impact of flow direction on flow pattern indicated in Figure 5.

4.2. The Corrugation Froude Number

The centrifugal force induced by the cross-corrugated profile is related to buoyancy by the corrugation Froude number $Fr_{\sim}$ defined in Eq. (1). The tilde used as index denotes the wavy profile of the corrugated plates. The corrugation Froude number contains the gravitational constant g and the velocity of the homogeneous two-phase mixture c_{2ph} given in Eq. (2) as the sum of liquid and gas superficial velocities [33]. The characteristic radius $\tilde{R}$ describes the curve imposed on the two-phase flow when crossing a sinusoidal corrugation as displayed in the bottom right diagram of Figure 1. The radius is set as the peak-to-peak amplitude of the corrugations or twice the corrugation depth $\tilde{R} = 2\,a$, as is substantiated in section 4.2.2.

$$Fr_{\sim} = \frac{c_{2ph}^2}{g\,\tilde{R}} \qquad \textit{Eq. (1)}$$

$$c_{2ph} = c_{S,liq} + c_{S,gas} \qquad \textit{Eq. (2)}$$

The impact of the centrifugal force vs. buoyancy on flow patterns is illustrated in Figure 5: If the corresponding Froude number is as low as $Fr_{\sim} < 1$, buoyancy and, thus, flow direction have a significant effect on flow patterns. If the Froude number $Fr_{\sim}$ is high, in contrast, the direction of flow has no impact which is observed for $Fr_{\sim} > 10$. For moderate Froude numbers $1 < Fr_{\sim} < 10$, the flow pattern classification is not much affected by buoyancy, but differences are visible in the photographs and attributed to the impact of buoyancy. The definition of the corrugation Froude number in Eq. (1) is derived in the following two subsections.

4.2.1. Force Balances

According to Wick and Tooby [34], the resultant force on a particle in rotating flow is termed "centrifugal buoyancy". The resultant force points in radial direction and is given in Eq. (3), where V_b is the bubble volume. The angular velocity Ω in Eq. (3) is replaced by $\Omega = c_{2ph}/\tilde{R}$, assuming the radial velocity roughly equal to the homogeneous mixture velocity given in Eq. (2). The sign of the resultant force becomes negative for bubbles driving them to the pivot point [26].

$$F_{rad} = V_b\,(\rho_{gas} - \rho_m)\,\Omega^2\,\tilde{R} = V_b\,(\rho_{gas} - \rho_m)\,c_{2ph}^2/\tilde{R} \qquad \textit{Eq. (3)}$$

The difference of buoyancy force to weight force points in vertical upward direction and is given in *Eq. (4)*. Since the bubbles belong to a swarm, the mean density ρ_m of the two-phase flow is inserted in Eq. (3) and *Eq. (4)* to represent the surrounding fluid.

$$F_{up} = V_b\,(\rho_m - \rho_{gas})\,g \qquad \textit{Eq. (4)}$$

The corrugation Froude number $Fr_{\sim}$ is defined as the ratio of centrifugal to gravitational buoyancy $Fr_{\sim} = |F_{rad}/F_{up}|$. Thus, the density difference and the bubble volume in Eq. (3) and *Eq. (4)* are cancelled out resulting in Eq. (1).

4.2.2. Characteristic Radius

The characteristic radius $\tilde{R}$ in Eq. (1) is perceived as the radius of a circular arc approximating the curved flow path over the sinusoidal corrugation. The mean two-phase flow path is presumed sinusoidal when projected into the yz-plane; see the dotted line in the bottom right diagram of Figure 1.

The radius of a circle R is deduced from the standard circle equation which is derived by three points on the circle. The three points are chosen at the maximum of the projected sinusoidal curve and at the distance of $0.2\,\lambda/\sin(\phi)$ from the maximum in positive and negative z-direction. With this, a general formulation of the circle radius approximating a sinusoidal corrugation profile is derived and given in Eq. (5).

$$R = 0.02\,[\lambda/sin\,(\phi)]^{\,2}\,\{a\,[1 - cos(0.4\,\pi)]\}^{-1} + 0.5\,a\,[1 - cos(0.4\,\pi)] \qquad Eq.\ (5)$$

Inserting the geometric parameters of the corrugated profile from Table 2 , the circle radius is calculated as $R = 2.5\,mm$. This is close to the characteristic radius $\tilde{R} = 2\,a = 2.4\,mm$ inserted in Eq. (1). Therefore, the characteristic radius is considered a simple and adequate means to estimate the centrifugal force induced by crossing the corrugations. For the given channel geometry, $\tilde{R} \cong R$ results in a deviation of 4% which has been included in the reported uncertainty of $Fr_{\sim}$. The circular arc with the radius $\tilde{R} \cong R$ is drawn as red line on the assumed two-phase flow path (dotted line) in the bottom right diagram of Figure 1.

The gas phase in bubbly flow (b, B) and Taylor-like bubbly flow (T) usually concentrates in the bubble-flow paths which are sketched in Figure 1. This is attributed to the centrifugal force caused by the bends in the xz-plane induced by the wave-crest contact points. However, the radius of the bends in the xz-plane cannot be approximated by only geometric considerations, because it seems to vary on the photographs depending on the flow rates of both phases. Also, this radius seems to be similar to or larger than the radius R in the yz-plane. Therefore, the radius of the bends in the xz-plane is not chosen as characteristic radius for $Fr_{\sim}$ because it exerts either similar or less centrifugal force on the two-phase flow compared to the radius R over the sinusoidal corrugations in the yz-plane.

5. EXPERIMENTAL RESULTS AND DISCUSSION

5.1. Flow Pattern Maps

The results of flow-pattern analysis are given as the flow pattern maps in Figure 6, presenting each flow direction separately in a diagram as well as combining all flow directions in one flow pattern map (bottom right). The abscissa and ordinate are the gas and liquid superficial velocities, respectively, calculated at actual operating conditions in the channel. Each letter in the diagrams represents a point of measurement classified as one of the flow patterns described in section 3. The error bars of the superficial velocities are smaller than the letters used as symbols and, therefore, are not shown. The empirical flow-pattern transitions are displayed as transparent shades. They were drawn to fit all flow directions in the best possible way and, thus, are the same in all diagrams in Figure 6.

Strikingly, the flow pattern classification yields very similar results for all flow directions [26]. This is attributed to the centrifugal force which dominates over buoyancy in many cases. Dashed contour lines of the corrugation Froude number $Fr_{\sim}$ show the ratio of both forces in Figure 6. For low corrugation Froude numbers, the flow patterns are more likely to differ with respect to flow direction. This is particularly true for $Fr_{\sim} < 1$ supported by the flow pattern of “stagnant gas phase" (S) only observed in vertical downward flow. For $Fr_{\sim} > 10$, however, flow patterns are independent of flow direction. At moderate Froude numbers of $1 < Fr_{\sim} < 10$, the influence of flow direction is marginal.

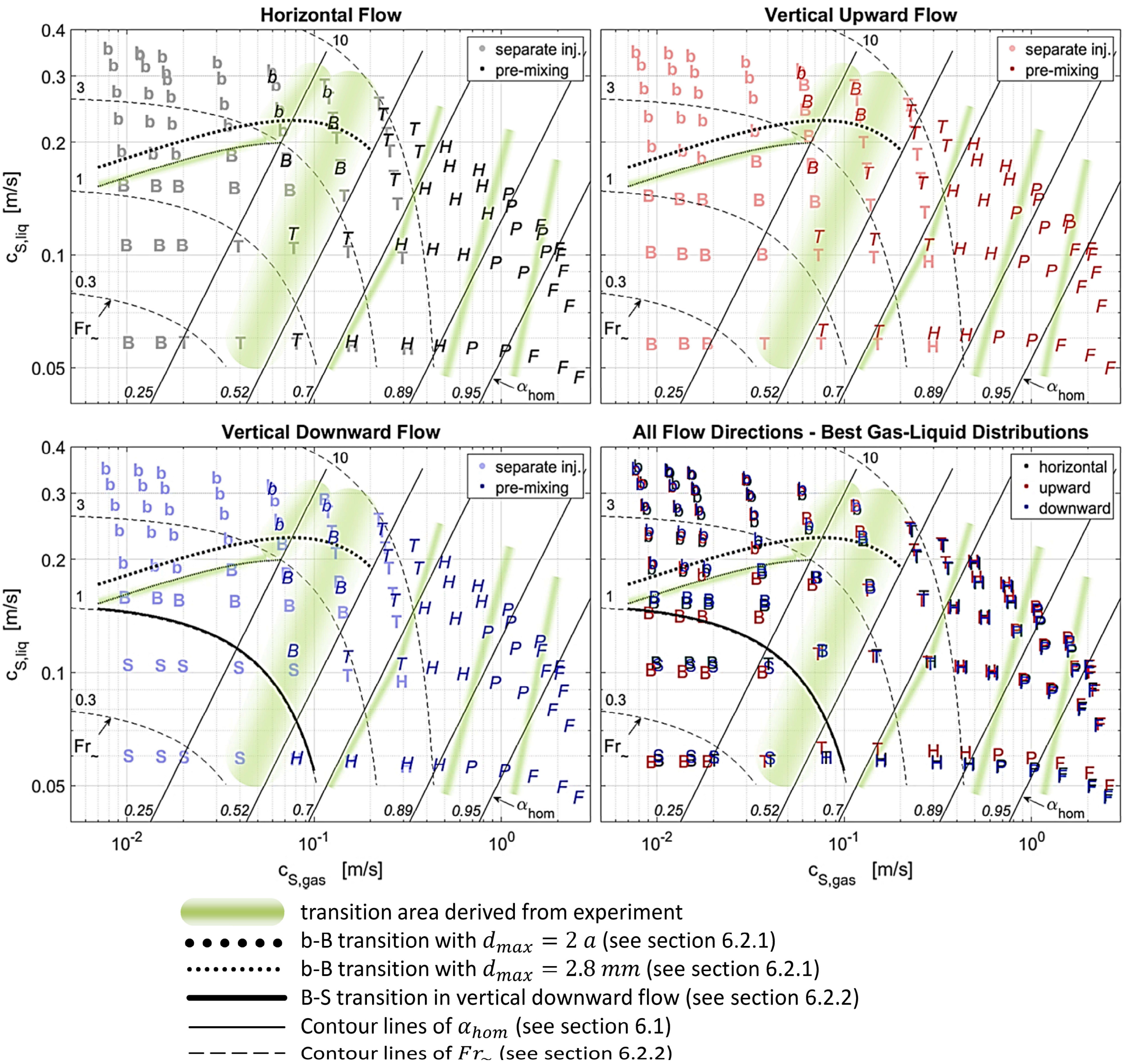

Figure 6: Flow pattern maps of different flow directions and combination of all flow directions

The diagrams of each flow direction distinguish by colour the two different injection methods explained in section 2.1 and displayed in Figure 3. The letters denoting the flow patterns are coloured brighter if gas and liquid are separately injected. The letters are coloured darker in the case of pre-mixing of both phases in the liquid-inlet tubes. For all three flow directions, the transition between bubbly (b or B) and intermediate flow with Taylor-like bubbles (T) is shifted a bit to the left if separate injection (bright colours) is used. Therefore, pre-mixing of the two phases in the liquid-inlet tubes is considered to yield a slightly better homogenization of the two-phase distribution, if a minimum gas superficial velocity (see section 2) is exceeded. This is explained as follows: For separate injection, gas and liquid enter the channel at opposite wave troughs which point at different directions according to the corrugation angle. Thus, the gas bubbles have a slight preference for one of the two bubble-flow paths emerging after injection, see Figure 3. As a consequence, more coalescence and earlier onset of Taylor-like bubbles occur due to a higher local void fraction in every other bubble-flow path in the case of separate injection, as shown by the zoom-in details of the photographs in Figure 3. Therefore, very small local maldistributions at the inlet can already impact flow patterns.

The transition between bubbly (b or B) and intermediate flow with Taylor-like bubbles (T) is marked as relatively wide area in the diagrams of Figure 6 in order to represent the observed sensitivity to small deviations of gas-liquid distribution. For the sake of clarity, the combined flow pattern map of all flow directions (bottom right diagram in Figure 6) only displays the best two-phase distributions, thus omitting the results of separate-injection when pre-mixing results are also available.

The flow pattern maps of this study diverge from published flow pattern maps of air-water flow, which also differ from each other, as demonstrated by Tao et al. [11]. One reason, indeed, could be different definitions of flow patterns. Also, varying corrugation angles and depths play a role. However, inlet effects have a major impact since they are responsible for the occurrence of oscillating flow patterns, see sections 5.2 and 1.2. Another main source of discrepancy is suspected in different assumptions about superficial gas velocity: In the present study, it is derived for each measurement point from the actual pressure and temperature measured at the same time in or near the channel. In contrast, although not perfectly re-traceable from the publications, some or maybe all of the previous research supposedly assumed standard conditions for the gas phase (see section 1.2). Due to the uncertainty regarding superficial gas velocities combined with non-specified operating conditions, published flow pattern maps are difficult to compare to each other and to this study.

Although the roughness of the micro-milled plates is higher than in common plate heat exchangers (see section 2.1), it is not assumed to affect flow patterns, agreeing with Taitel et al. [14], since the flow is adiabatic. At all measurement points, the plate surfaces are entirely wetted and at least 2% of the channel volume is filled with liquid, thus, film thickness is most likely always well above maximum roughness. The impact of wall roughness on pressure drop is considered negligible for a plate heat exchanger, since its friction factor is much higher [27], due to many directional changes, than compared to a tube with a similar hydraulic diameter and a large influence of wall friction. If phase change occurs, however, roughness is agreed to affect heat transfer and pressure drop [21].

5.2. The Absence of Slug or Churn Flow

Contrasting with other studies [9,10,19], so-called slug or churn flow is not observed in the present experiments, i. e. periodically changing gas-liquid proportions across the whole channel width (see Table 1) did not occur. Since the mentioned studies had tube inlets, the phenomenon can be attributed to intermittent flow in the inlet tube. Also using a mixing chamber does not preclude slugging, see Grabenstein et al. [7], Jiang and Bai [21] discussed in section 1.2. The absence of slugging in the current study is attributed to the implementation of a uniform and steady gas-liquid injection.

None of the research cited in section 1.2 explained why slug or churn flow should occur in a cross-corrugated channel. In slugging pipe flow, the Taylor bubbles are formed quickly because bubbles change their speed with increasing size, thus, accelerating coalescence further and resulting in local phase separation. Pressure oscillations occur when the liquid slugs become shorter and collapse [15]. In cross-corrugated channels, however, bubbles cannot accelerate in the same manner as in tubes because the centrifugal forces, induced by the helical flow path, hold them back (section 4.1). The Taylor-like bubbles and their liquid barriers do not expand over the whole channel cross-section and, therefore, are not responsible for pressure oscillations if the liquid barriers are destroyed. Consequently, so-called slug or churn flow in plate heat exchangers must be attributed to periodic changes of the gas-liquid distribution in the inlet tube, see also [10] and [22].

Intermittent phenomena in the channel can be induced by various sources, not only in the inlet, but also in the test plant. This was encountered in the preliminary experiments to this study, as described in section 2.2. However, not all intermittent phenomena seem to have been eliminated: At high gas and liquid flow rates, fluctuations of gauge and differential pressure are measured while local variations of film waviness are observed. The turbulence in film flow changes in different regions of the channel without a clear pattern, suggesting that external pressure fluctuations are randomly transported into the channel via its numerous inlet and outlet openings. Possible sources are slugging in the outlet tubing or disturbances of the water surface in the storage tank, still present at very high mixture velocities, or a combination of both. The observation that flow patterns and pressure fluctuations are affected by changes at the test plant supports this hypothesis. Moreover, pressure oscillations located in various parts of the experimental facility are assumed to mutually reinforce each other [26].

6. MODELLING FLOW PATTERN TRANSITIONS

A mechanistic flow pattern model for tubes was introduced by Taitel et al. [14,15] and developed further by several studies resulting in the “unified model” of Barnea [16] to include variable inclination angles. Several of their assumptions are adopted here to model flow pattern transitions in cross-corrugated channels.

In the following sections, the transition lines between the flow patterns are modelled individually. The transition models are grouped according to the supposed underlying physical parameters. Therefore, the first transition models are based upon the void fraction (section 6.1), and the subsequent transition models are based on the energy dissipation rate (section 6.2). In each subsection, at first, the equations and adopted assumptions from the literature are explained (if available). Subsequently, changes to the said assumptions (if thought necessary) are proposed and (optionally) new assumptions are introduced. Finally, the experimental observations are discussed in the light of the proposed modelling.

The proposed transition modelling is not restricted to certain plate geometries – as long as they induce permanent directional changes of the two-phase mixture, thus adopting a helical flow path and reducing the impact of buoyancy (see section 4.1). The helical-flow condition is presumably fulfilled by chevron and herringbone-type plate heat exchangers with a corrugation angle of at least 60°. Experimental validation is needed for low corrugation angles which might not induce helical flow. As attributed to the centrifugal forces, most of the following modelling is based on the assumption of homogeneous two-phase flow – which was shown to be valid or at least a reasonable approximation for the cross-corrugated channel if the flow rates are not too low [23].

The second main presumption is a uniform gas-liquid distribution across the channel width. This indeed might be difficult to achieve in common plate heat exchangers, especially at low flow rates. However, if real two-phase distributions were known, the modelling could probably be accommodated. If the inlet is characterized by a conventional porthole, modelling the flow patterns in the inlet pipe according to Taitel et al. [14] or Barnea [16] could be useful to predict oscillating flow patterns (i. e. slug or churn flow) in the plate heat exchanger.

Phase change and mass transfer between the phases are not accounted for in this simple model, but of course they need to be included in an incremental model of a real plate heat exchanger.

6.1. Modelling Based on the Homogeneous Void Fraction

The homogeneous void fraction α_{hom} given in Eq. (6) represents the portion of the volumetric gas content in the channel, presuming the homogeneous model, i. e. the absence of slip [33].

$$\alpha_{hom} = \frac{c_{S,gas}}{c_{S,liq} + c_{S,gas}} \qquad \text{Eq. (6)}$$

The homogeneous void fractions are displayed as solid contour lines in the flow pattern maps of Figure 6. The flow pattern transitions modelled on the basis of homogeneous void fractions are summarized in Table 3.

Table 3. Flow pattern transitions based on homogeneous void fraction

α_{hom}	Transition line	Section	Model assumptions
0.25	b/B ↔ B/T	6.1.1	Distance of ½ radius between monodisperse round bubbles [16]
0.52	B/T ↔ T	6.1.1	Maximum packing density of monodisperse round bubbles [16]
0.70	T ↔ H	6.1.2	Local film ratio 0.38 according to Eq. (8); similar to definition of "H" in section 3.2 (min. 40% of projected area of two-phase flow)
(0.89)	(H ↔ P)	(6.1.2)	(Empirical value, local film ratio was not pre-defined for "P")
0.95	P ↔ F	6.1.2	Local film ratio 0.90 according to Eq. (8); similar to definition of "F" in section 3.3 (min. 90% of projected area of two-phase flow)

6.1.1. Low vs. Maximum "Packing Density" in Bubble Swarms – Transitions b/B-B/T and B/T-T

Taitel et al. [15] and Barnea [16] made the following rather geometrical assumptions for two-phase flow in tubes: Agglomeration of bubbles is prevented if they can keep a distance of at least half their radius to each other. Presuming a swarm of monodisperse round bubbles arranged in a cubic lattice, the maximum homogeneous void fraction to ensure bubbly flow is $\alpha_{hom} = 0.25$. Increasing gas flow rates result in closer bubble spacing and an increase of coalescence. The maximum packing in a bubble swarm of the same kind is reached at a homogeneous void fraction of $\alpha_{hom} = 0.52$. In the region between both void fractions ($0.25 < \alpha_{hom} < 0.52$), disperse bubbly flow exists in the case of high liquid flow rates which provide strong turbulent velocity fluctuations and cause sufficient bubble breakup to compensate for coalescence. If bubble breakup due to turbulent velocity fluctuations is small, Taylor-bubbles separated by liquid-slugs are formed in the tube. At higher homogeneous void fractions ($\alpha_{hom} > 0.52$), Taylor bubbles are sure to form because the bubble density exceeds the suspected maximum packing of bubbles.

The experimental results of the current study confirm both of the theoretical boundaries of Taitel et al. [15] and Barnea [16] for all flow directions as shown in Figure 6: If the homogeneous void fraction is less than 0.25, only bubbly flow (b, B) is observed – with the exception of the stagnant gas phase (S) for downward flow at very low corrugation Froude numbers (< 1). At homogeneous void fractions between 0.25 and 0.52, both bubbly flow (B) and Taylor-like bubbles (T) are observed. Taylor-like bubbles (T) dominate at low Froude numbers and higher void fractions. However, void fractions above 0.52 rule out bubbly flow.

6.1.2. Local Film Flow – Transitions T-H and P-F

A new model is proposed to estimate the amount of local film flow described in the flow pattern definitions of sections 3.2 and 3.3: The two-phase volumetric flow rate $\dot{V}_{2ph}$ is imagined as the sum of local bubbly flow $\dot{V}_{bub}$ and local film flow $\dot{V}_{film}$, the latter including Taylor-like bubbles. The volume of the liquid in local film flow is assumed much smaller compared to the liquid volume in local bubbly flow. Therefore, the volumetric flow rate of the liquid $\dot{V}_{liq}$ is entirely allocated to local bubbly flow $\dot{V}_{bub}$. The homogeneous void fraction of local bubbly flow is assumed as $\alpha_{bub} = 0.52$, that is the maximum bubble packing as given in section 6.1.1. These considerations result in Eq. (7).

$$\dot{V}_{2ph} = \dot{V}_{bub} + \dot{V}_{film} = \left(\alpha_{bub}\dot{V}_{bub} + \dot{V}_{liq}\right) + \dot{V}_{film} \qquad \textit{Eq. (7)}$$

$$r_{film} = \frac{\dot{V}_{film}}{\dot{V}_{2ph}} = \frac{\alpha_{hom} - \alpha_{bub}}{1 - \alpha_{bub}} \qquad \textit{Eq. (8)}$$

The “local film flow ratio” r_{film} is defined in Eq. (8) as the proportion of the volumetric flow rate of the local film flow to total two-phase flow. Transforming Eq. (7) according to this definition, the local film flow ratio r_{film} is derived as given in Eq. (8), employing the relations $\dot{V}_{bub} = (1 - r_{film})\dot{V}_{2ph}$ and $\dot{V}_{liq} = (1 - \alpha_{hom})\dot{V}_{2ph}$. This simple model of local film flow explains the gradual character of the intermediate flow pattern transitions by referring to the homogeneous void fraction which also increases gradually. However, the simple model neglects the liquid film in local film flow and the existence of slip which was investigated in [23]. Also, the model does not account for Taylor-like bubbles at void fractions of $\alpha_{hom} \leq 0.52$.

In the experimental flow pattern maps of Figure 6, the empirical transitions to heterogeneous flow (H), partial film flow (P) and full film flow (F) are found to roughly agree with the contour lines of $\alpha_{hom} = 0.70$, $\alpha_{hom} = 0.89$ and $\alpha_{hom} = 0.95$, respectively. The proposed local-film flow model is able to explain the similarities between two of the contour lines and the respective empirical transitions: First, with Eq. (8), a local film flow ratio of $r_{film} = 0.38$ is calculated for a homogeneous void fraction of $\alpha_{hom} = 0.70$ which corresponds to the experimental transition from Taylor-like bubbly flow (T) to heterogeneous flow (H) in Figure 6. The local film flow ratio of 0.38 is also close to the visually assessed minimum of 40% of the projected area of the two-phase flow, as previously defined for heterogeneous flow (H) in section 3.2. Secondly, according to Eq. (8), the local film flow ratio is $r_{film} = 0.9$ for the void fraction of $\alpha_{hom} = 0.95$. This void fraction corresponds to the transition line from partial film flow (P) to full film flow (F) in Figure 6. In section 3.3, full film flow (F) is pre-defined to contain a maximum of 10% local bubbly flow or a minimum of 90% local film flow with respect to the projected two-phase area. Thirdly, as to the transition from heterogeneous flow (H) to partial film flow (P), however, no area proportion of local film flow has been previously defined for partial film flow. Nonetheless, all three contour lines of α_{hom} are included in Table 3.

Finally, additional considerations need to justify the comparison of the local film flow ratio, which is modelled as a volumetric fraction, and the visually assessed projected area of the two-phase flow: The channel height could be assumed roughly constant when only regarding the two-phase flow. This is reasonable because the liquid-filled volumes near the wave-crest contact points can be neglected being small compared to the rest of the channel. Since these volumes are always filled with pure liquid, their projected areas are also not included in the projected two-phase area.

6.2. Modelling Based on the Energy Dissipation Rate

The energy dissipation rate ϵ in a tube can be determined, according to Taitel et al. [15] and others, by the frictional pressure drop as given in Eq. (9), using the homogeneous mixture velocity of Eq. (2). The friction factor ζ in Eq. (9) is defined according to [27].

$$\epsilon = \frac{\Delta p_{fric,2ph}}{L} \frac{c_{2ph}}{\rho_m} = \zeta \, \frac{1}{2} \frac{c_{2ph}^3}{D_h} \qquad \text{Eq. (9)}$$

The correlation of the friction factor ζ is given in Eq. (10) and was derived from own measurements of single- and two-phase pressure drop in the cross-corrugated channel as published in [23].

$$\zeta = 19.9 \left(\frac{c_{2ph} \, D_h}{\nu_{liq}} \right)^{-0.225} \qquad \text{Eq. (10)}$$

The flow pattern transitions modelled on the basis of the energy dissipation rate are summarized in Table 4.

Table 4. Flow pattern transitions based on dissipation rate

Characteristic length	Section	Transition line	Model assumptions
$d_{max} = 2.4 \, mm = 2 \, a$	6.2.1	b-B, theory	Eq. (9) - Eq. (12), see Barnea [16] and Hinze [35]; geometric limit: $d_{max} = 2 \, a$; ε from pressure drop
$d_{max,exp} = 2.8 \, mm$	6.2.1	b-B, experiment	Eq. (9) Eq. (11)- Eq. (12); d_{max} adapted to experimental transition; moderate bubble deformation permitted
$w_{max} = D_h/2$	6.2.2	B-S, down-flow	Eddy of scale $w_0 = D_h$ has to split to fit Hinze model [35]; if eddies w_{max} too weak: no bubble breakage

6.2.1. Maximum Round Bubble Diameter – Transition b-B

Barnea [16] and Taitel et al. [15] stated a transition line distinguishing “dispersed bubbly flow” from “bubbly flow” based on Hinze [35] who predicted the maximum drop size in a stirred vessel by the rate of turbulent energy dissipation per unit mass. The model of Hinze [35] presumes a very low void fraction and only accounts for fluid particle breakup, but not for coalescence. The model equation of Hinze is given in Eq. (11) comprising the surface tension σ and the liquid density ρ_{liq}.

$$d_{max} = k \left(\frac{\sigma}{\rho_{liq}} \right)^{3/5} \epsilon^{-2/5} \qquad \text{Eq. (11)}$$

$$k = 0.725 + 4.15 \, \alpha_{hom}^{0.5} \qquad \text{Eq. (12)}$$

In order to account for higher void fractions, Barnea, Shoham et al. [36] introduced an empirical modification of the constant k in Eq. (11) by the expression in Eq. (12) referring to Calderbank [37]. Although the measurements of [37] were limited to void fractions below 0.1 in an aerated stirred tank, Barnea et al. [16,36] utilized the modified constant k in Eq. (12) to model the flow pattern transition with void fractions up to $\alpha_{hom} \leq 0.52$.

Due to geometric restrictions of cross-corrugated channels, an adjustment to the assumptions of the literature is reasonable: The maximum bubble diameter d_{max} defined by Barnea [16], which is not presented here, is not applicable to cross-corrugated channels because the size of non-deformed bubbles is already limited to twice the corrugation depth: Bubbles bigger than $d_{max} = 2\ a$ are not able to pass the cross-corrugated channel without being deformed. The cross-section in the middle of the bubble-flow path and the channel height in the bubble-flow path, both given in the bottom diagrams of Figure 1, illustrate this geometrical constraint.

The modified transition line defined in Eq. (9) to Eq. (12) with $d_{max} = 2\ a = 2.4\ mm$ and $\alpha_{hom} \leq 0.52$ is displayed in the experimental flow pattern maps of Figure 6 as fat dotted line. The model agrees quite well with the experimental data, although the theoretical transition line is located a bit above the empirical transition between the small roundish bubbles (b) and the blob-like bubbles (B).

In order to improve agreement between model and experiment, the maximum bubble diameter was adapted to $d_{max,exp} = 2.8\ mm$ (+17%) and the void fraction to $\alpha_{hom} \leq 0.25$. This empirically adapted model, also calculated with Eq. (9) to Eq. (12), is drawn as thin dotted line in the flow pattern maps of Figure 6. The increase of the maximum bubble size is consistent with the definition of the flow pattern "B" in section 3.1 because the identification of blob-like bubbles (B) as opposed to small roundish bubbles (b) requires frequent appearance of large, clearly deformed bubbles in the photographs. Both versions of the b-B transition line are given in Table 4.

6.2.2. Kinetic Energy of Secondary Eddies – Transition B-S in Down-Flow

The model of Hinze [35] is based on the energy distribution law stated in the theory of locally isotropic turbulence by Kolmogorov [38]. Summarizing the theory, Shinnar and Church [39] stated the primary eddies to be of main-flow scale and to decompose forming smaller eddies which completely lack directional information. The primary eddies contain most of the kinetic energy and transfer it during decomposition to smaller eddies. The energy distribution law of Kolmogorov is restricted to eddies much smaller than the primary eddy. Hinze [35] assumed the scale of the eddy breaking a fluid particle equal to the particle diameter.

Applying the aforementioned models to the cross-corrugated channel, the following own logical conclusions are drawn. First, the energy distribution law is not valid for eddies of scale $\mathrm{w} > D_h/2$ in the cross-corrugated channel: The scale of the primary eddies in the channel is roughly equal to the hydraulic diameter $w_0 = D_h$. They have to disintegrate at least once, but rather several times, to lose their directional information. Second, if eddies of size $w_{max} = D_h/2$ do not have enough energy to break up bubbles, the overall turbulent kinetic energy is too weak to cause bubble breakage at all, and, therefore, only coalescence occurs in the channel.

The following own adjustment to the literature model is introduced in order to evaluate the possibility of bubble breakage: The characteristic length of the Hinze model d_{max} in Eq. (11) is replaced by the size of the largest eddy assumed responsible for bubble breakage: $w_{max} = D_h/2$. Furthermore, the constant in Eq. (11) is set to $k = 1.15$ according to theory and experiments of bubble breakage by Sevik and Park [40]; as previously suggested by Taitel et al. [15]. The transition model is listed in Table 4.

The transition line combining Eq. (9) to Eq. (11) with the adjusted constants is displayed as fat black line in the experimental flow pattern map of vertical downward flow and in the map combining all flow directions in Figure 6. This transition line suggests that bubble breakage is absent in the case of a supposed homogeneous flow with very low gas and liquid superficial velocities. Horizontal and upward flow are not affected by the lack of bubble breakage, since the gas phase is uniformly distributed at the entrance and the collision probability with other bubbles is low due to the helical flow paths. In vertical down-flow, however, the gas phase accumulates in the channel at very low flow rates not overcoming buoyancy ($Fr_{\sim} < 1$), thus, invalidating the homogeneous model. The liquid accelerates, because most of the channel is blocked by the gas, until it has enough kinetic energy to split up the big gas bubbles trapped in the recirculation zones. Smaller bubbles, fragments of the break-ups, are transported downwards by the liquid. Hence, the steady-state flow pattern of the "stagnant gas phase" (S) is formed.

It is not surprising that the transition line B-S in vertical down-flow is equal to a contour line of $Fr_{\sim} = const.$ in Figure 6 because both Eq. (11) and Eq. (1) are rearranged to the form $c_{S,liq} = const. - c_{S,gas}$ in order to be plotted in the flow pattern maps. The closeness of the B-S transition line to $Fr_{\sim} = 1$ suggests the chosen constants and model assumptions to be coherent. The dominance of buoyancy is a prerequisite of the gas accumulation because it prevents big gas bubbles from being transported downwards at low flow rates.

7. CONCLUSIONS

Flow patterns maps are derived from experiments in a cross-corrugated channel with a uniform gas-liquid distribution across the channel width, obtained by a special inlet design. The flow pattern transitions have been modelled successfully. The findings are listed as follows:

- A steady and uniform two-phase distribution is accomplished by gas-liquid injection via nozzles. Even small changes to the injection can affect the two-phase distribution in the channel and, hence, be detectable in the flow patterns. In order to eliminate external sources of unsteady two-phase phenomena, great care has to be taken with the design of the test plant.

- The superficial velocity of the gas phase and the void fraction are calculated with respect to the actual operating conditions in the channel. This is required in order to interpret the data with respect to known two-phase phenomena such as bubble breakage and coalescence.

- The variation of flow direction has no effect on flow patterns in most cases. As an exception to this, very low flow rates in vertical downward flow induce a unique flow pattern characterized by a great amount of stagnant gas phase.

- The corrugation Froude number is introduced to quantify the relation of centrifugal force to buoyancy in the helical flow path, which is enforced by the cross-corrugated geometry. This Froude number explains the varying impact of flow direction on flow patterns with respect to flow rates.

- So-called slug or churn flow is not observed in the experiments, in contrast to other studies investigating plate heat exchangers. Slugging is caused by two-phase maldistribution in the inlet which is enhanced by the commonly large portholes of plate heat exchangers.

- Flow pattern transitions are modelled based on void fraction and energy dissipation rate. The modelled transitions agree well with the experimental flow pattern maps. Model assumptions for bubbly flow in tubes are adapted. A simple model of the local film flow is added. A proposed condition for bubble breakage accounts for gas accumulation at slow down-flow. The definitions of flow patterns influence the experimental flow pattern maps as well as the modelling of flow pattern transitions.

Due to simplicity of the model assumptions, the validity of the model is assumed to apply regardless of plate geometry and material properties – in the case that the following idealizing conditions hold true:

- Continuously swirling flow is induced by the channel geometry.
- The two-phase distribution across the channel width is steady and uniform.
- Gas properties are calculated at operating conditions.
- Coalescence is not influenced by additives or contaminants.
- The pressure drop of the channel is known.
- Phase change and mass transfer are negligible.

Local void fraction is fundamental to the proposed modelling of flow pattern transitions. Since the two-phase distributions in real plate heat exchangers are in most cases not uniform, knowledge of the local gas-liquid proportions, and modelling of flow patterns in the inlet pipe should be incorporated in order to predict flow patterns correctly.

NOMENCLATURE

a	corrugation depth (mm)	r_{film}	ratio of local film flow (-)
B	channel width (mm)	$\dot{V}$	volumetric flow rate (m³/s)
c_{2ph}	homogeneous mixture velocity (m s-1)	V_b	volume of a bubble (m³)
$c_{S,Gas}$	superficial gas velocity (m s^{-1})		
$c_{S,Liq}$	superficial liquid velocity (m s^{-1})		
d_{max}	maximum bubble diameter (mm)	α_{hom}	homogeneous void fraction (-)
D_h	hydraulic diameter (mm)	ϵ	dissipation rate (W kg-1)
F	force (N)	ζ	friction factor (-)
$Fr_{\sim}$	corrugation Froude number (-)	λ	wave length (mm)
g	gravitational constant (m s²)	ν	kinematic viscosity (m^2 s^{-1})
L	channel length (mm)	ρ_m	mean two-phase density (kg/m^{-3})
w	eddy size (mm)	σ	surface tension (N/m)
$\Delta p_{fric,2ph}$	pressure drop (bar)	ϕ	corrugation angle (°)
$\tilde{R}$	characteristic radius (mm)	Ω	angular velocity (s^{-1})

REFERENCES

[1] X. Tao, C.A. Infante Ferreira, Heat transfer and frictional pressure drop during condensation in plate heat exchangers: Assessment of correlations and a new method, International Journal of Heat and Mass Transfer 135 (2019) 996–1012.

[2] Z.H. Ayub, T.S. Khan, S. Salam, K. Nawaz, A.H. Ayub, M.S. Khan, Literature survey and a universal evaporation correlation for plate type heat exchangers, International Journal of Refrigeration 99 (2019) 408–418.

[3] F. Táboas, M. Vallès, M. Bourouis, A. Coronas, Flow boiling heat transfer of ammonia/water mixture in a plate heat exchanger, International Journal of Refrigeration 33 (2010) 695–705.

[4] J. Cerezo, R. Best, R.J. Romero, A study of a bubble absorber using a plate heat exchanger with NH3–H2O, NH3–LiNO3 and NH3–NaSCN, Applied Thermal Engineering 31 (2011) 1869–1876.

[5] M. Suresh, A. Mani, Heat and mass transfer studies on a compact bubble absorber in R134a-DMF solution based vapour absorption refrigeration system, International Journal of Refrigeration 36 (2013) 1004–1014.

[6] V. Grabenstein, Experimentelle Untersuchung und Modellierung der Kondensation in Plattenwärmeübertragern, Dissertation, Gottfried Wilhelm Leibniz Universität Hannover, 2014.

[7] V. Grabenstein, A.-E. Polzin, S. Kabelac, Experimental investigation of the flow pattern, pressure drop and void fraction of two-phase flow in the corrugated gap of a plate heat exchanger, International Journal of Multiphase Flow 91 (2017) 155–169.

[8] C. Tribbe, H.M. Müller-Steinhagen, Gas/Liquid Flow in Plate-and-Frame Heat Exchangers - Part I: Pressure Drop Measurements, Heat Transfer Engineering 22 (2001) 5–11.

[9] C. Tribbe, H.M. Müller-Steinhagen, Gas/Liquid Flow in Plate-and-Frame Heat Exchangers - Part II: Two-Phase Multiplier and Flow Pattern Analysis, Heat Transfer Engineering 22 (2001) 12–21.

[10] P. Vlasogiannis, G. Karagiannis, P. Argyropoulos, V. Bontozoglou, Air–water two-phase flow and heat transfer in a plate heat exchanger, International Journal of Multiphase Flow 28 (2002) 757–772.

[11] X. Tao, M.P. Nuijten, C.A. Infante Ferreira, Two-phase vertical downward flow in plate heat exchangers: Flow patterns and condensation mechanisms, International Journal of Refrigeration 85 (2018) 489–510.

[12] D. Winkelmann, Condensation of Pure Refrigerants and Their Zeotropic Mixtures in Plate Heat Exchangers, Toward a Better Design Method, Dissertation, TU Berlin, 2010.

[13] V. Grabenstein, S. Kabelac, Experimental and theoretical analysis of the local condensation heat transfer in a plate heat exchanger, J. Phys.: Conf. Ser. 395 (2012) 12169.

[14] Y. Taitel, A.E. Dukler, A model for predicting flow regime transitions in horizontal and near horizontal gas-liquid flow, AIChE Journal 22 (1976) 47–55.

[15] Y. Taitel, D. Barnea, A.E. Dukler, Modelling flow pattern transitions for steady upward gas-liquid flow in vertical tubes, AIChE J. 26 (1980) 345–354.

[16] D. Barnea, A unified model for predicting flow-pattern transitions for the whole range of pipe inclinations, International Journal of Multiphase Flow 13 (1987) 1–12.

[17] Y. Shiomi, S. Nakanishi, T. Uehara, Characteristics of two-phase flow in a channel formed by chevron type plates, Experimental Thermal and Fluid Science 28 (2004) 231–235.

[18] H. Asano, N. Takenaka, T. Wakabayashi, T. Fujii, Visualization and void fraction distribution of downward gas–liquid two-phase flow in a plate heat exchanger by neutron radiography, Nuclear Instruments and Methods in Physics Research Section A: Accelerators, Spectrometers, Detectors and Associated Equipment 542 (2005) 154–160.

[19] K. Nilpueng, S. Wongwises, Two-phase gas–liquid flow characteristics inside a plate heat exchanger, Experimental Thermal and Fluid Science 34 (2010) 1217–1229.

[20] C.-Y. Yang, Y.-H. Lin, F.-Y. Meng, G.-C. Li, Flow distribution of two-phase refrigerant in plate heat exchangers, Keynote E1-We-1, in: Proceedings of the 24th IIR International Congress of Refrigeration, 2015.

[21] C. Jiang, B. Bai, Flow patterns and pressure drop of downward two-phase flow in a capsule-type plate heat exchanger, Experimental Thermal and Fluid Science 103 (2019) 347–354.

[22] H. Asano, N. Takenaka, T. Fujii, Flow characteristics of gas–liquid two-phase flow in plate heat exchanger, Experimental Thermal and Fluid Science 28 (2004) 223–230.

[23] S. Buscher, Pressure drop and void fraction of vertical and horizontal adiabatic two-phase flow in a plate heat exchanger single channel with uniform gas-liquid distribution, Paper ID 468, in: Proceedings of the 25th IIR International Congress of Refrigeration, 2019.

[24] J. Cerezo, R. Best, M. Bourouis, A. Coronas, Comparison of numerical and experimental performance criteria of an ammonia–water bubble absorber using plate heat exchangers, International Journal of Heat and Mass Transfer 53 (2010) 3379–3386.

[25] Y. Tae Kang, A. Akisawa, T. Kashiwagi, Analytical investigation of two different absorption modes, International Journal of Refrigeration 23 (2000) 430–443.

[26] S. Buscher, Flow patterns of vertical and horizontal adiabatic two-phase flow in a plate heat exchanger single channel with uniform gas-liquid distribution, Paper ID 512, in: Proceedings of the 25th IIR International Congress of Refrigeration, 2019.

[27] H. Martin, Pressure drop and heat transfer in plate heat exchangers, N6, in: VDI-GVC (Ed.), VDI Heat Atlas, 2nd ed., Springer, Berlin, Heidelberg, New York, 2010, 1515-1521.

[28] B. Wu, M. Firouzi, T. Mitchell, T.E. Rufford, C. Leonardi, B. Towler, A critical review of flow maps for gas-liquid flows in vertical pipes and annuli, Chemical Engineering Journal 326 (2017) 350–377.

[29] Joint Committee for Guides in Metrology (JCGM), Evaluation of measurement data - Guide to the expression of uncertainty in measurement: GUM 1995 with minor corrections JCGM 100:2008, 2010.

[30] W.W. Focke, P.G. Knibbe, Flow visualization in parallel-plate ducts with corrugated walls, J. Fluid Mech. 165 (1986) 73.

[31] K. Usui, S. Aoki, A. Inoue, Flow Behavior and Pressure Drop of Two-Phase Flow through C-Shaped Bend in Vertical Plane, (I), Journal of Nuclear Science and Technology 17 (1980) 875–887.

[32] R.J. Da Silva Lima, J.R. Thome, Two-phase flow patterns in U-bends and their contiguous straight tubes for different orientations, tube and bend diameters, International Journal of Refrigeration 35 (2012) 1439–1454.

[33] Y. Taitel, D. Barnea, J.R. Thome, Modeling of gas liquid flow in pipes, Encyclopedia of two-phase heat transfer and flow Fundamentals and methods 1, World Scientific, New Jersey, 2016.

[34] G.L. Wick, P.F. Tooby, Centrifugal buoyancy forces, Am. J. Phys. 45 (1977) 1074–1076.

[35] O.J. Hinze, Fundamentals of the Hydrodynamic Mechanism of Splitting in Dispersion Processes, AIChE Journal 1 (1955) 289–295.

[36] D. Barnea, O. Shoham, Y. Taitel, Flow pattern transition for vertical downward two phase flow, Chemical Engineering Science 37 (1982) 741–744.

[37] P.H. Calderbank, Physical Rate Processes in Industrial Fermentation, Part I The Interfacial Area in Gas-Liquid Contacting with Mechanical Agitation, Trans. Instn. Chem. Engrs. 36 (1958) 443–463.

[38] A.N. Kolmogorov, Dissipation of Energy in the Locally Isotropic Turbulence: [English translation by V. Levin, in: Proc. R. Soc. Lond. A 434, 1991, 15-17], Doklady Akademiia Nauk SSSR 32 (1941) 16–18.

[39] R. Shinnar, J.M. Church, Statistical Theories of Turbulence in Predicting Particle Size in Agitated Dispersions, Ind. Eng. Chem. 52 (1960) 253–256.

[40] M. Sevik, S.H. Park, The Splitting of Drops and Bubbles by Turbulent Flow, Journal of Fluids Engineering 95 (1973) 53–60.